JBIC Journal of Biological Inorganic Chemistry (2020) 25:635–645
https://doi.org/10.1007/s00775-020-01786-z

ORIGINAL PAPER

High-resolution crystal structures of a "half sandwich"-type Ru(II) coordination compound bound to hen egg-white lysozyme and proteinase K

Lykourgos Chiniadis[1,2] · Ioannis Bratsos[3] · Kostas Bethanis[2] · Michael Karpusas[2] · Petros Giastas[4] · Athanasios Papakyriakou[1]

Received: 12 February 2020 / Accepted: 24 March 2020 / Published online: 8 April 2020

Abstract

The high-resolution X-ray crystal structures of the adducts formed between the "half sandwich"-type Ru(II) *coordination* compound $[Ru^{II}$(1,4,7-trithiacyclononane)(ethane-1,2-diamine)Cl$]^+$ and two proteins, namely hen egg-white lysozyme and proteinase K, are presented. The structures unveil that upon reaction with both enzymes the Ru(II) compound is coordinated by solvent-exposed aspartate residues after releasing the chloride ligand (Asp101 in lysozyme, Asp200 and Asp260 in proteinase K), while retaining the two chelating ligands. The adduct with Asp101 residue at the catalytic cleft of lysozyme is accompanied by residue-specific conformational changes to accommodate the Ru(II) fragment, whereas the complexes bound at the two calcium-binding sites of proteinase K revealed minimal structural perturbation of the enzyme. To the best of our knowledge, proteinase K is used here for the first time as a model system of protein metalation and these are the first X-ray crystal structures of protein adducts of a Ru(II) *coordination* compound that maintains its coordination sphere almost intact upon binding. Our data demonstrate the role of ligands in stabilizing the protein adducts via hydrophobic/aromatic or hydrogen-bonding interactions, as well as their underlying role in the selection of specific sites on the electrostatic potential surface of the enzymes.

Keywords Ruthenium anticancer compounds · X-ray crystallography · Lysozyme (HEWL) · Proteinase K · Protein ruthenation

Introduction

In the field of metal-based anticancer drugs, ruthenium compounds have shown good promise as potential alternatives to the approved Pt(II)-based drugs cisplatin, carboplatin, and oxaliplatin [1, 2]. Ever since the almost contemporary introduction of two Ru(III) compounds into clinical trials, namely NAMI-A [3] and KP1019 [4],

Data deposition: Atomic coordinates and structure factors have been deposited in the Protein Data Bank, https://www.rcsb.org/ (PDB ID codes 6TVL and 6TXG).

Electronic supplementary material The online version of this article (https://doi.org/10.1007/s00775-020-01786-z) contains supplementary material, which is available to authorized users.

✉ Petros Giastas
petrosgiastas@gmail.com

✉ Athanasios Papakyriakou
thpap@bio.demokritos.gr

[1] Institute of Biosciences and Applications, National Centre for Scientific Research "Demokritos", 15341 Athens, Greece

[2] Department of Biotechnology, School of Applied Biology and Biotechnology, Agricultural University of Athens, 11855 Athens, Greece

[3] Institute of Nanoscience and Nanotechnology, National Centre for Scientific Research "Demokritos", 15341 Athens, Greece

[4] Department of Neurobiology, Hellenic Pasteur Institute, 11521 Athens, Greece

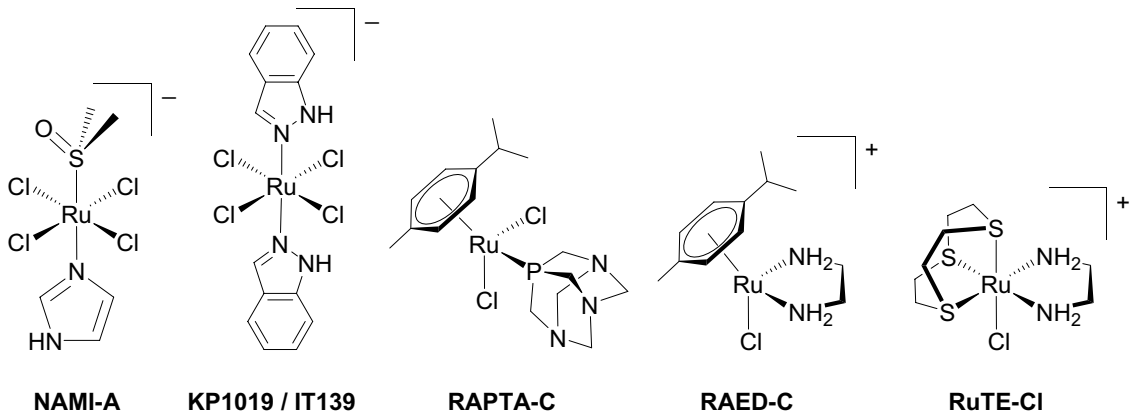

Fig. 1 Structures of the anticancer Ru(III) complexes NAMI-A (imidazolium salt), KP1019 (indazolium salt), or IT139 (Na^+ salt), the organometallic half-sandwich Ru(II) complexes RAPTA-C and RAED-C (both PF_6^- salts), and the Ru(II) *coordination* complex RuTE-Cl (as $CF_3SO_3^-$ salt) used here

which was later replaced by its more soluble sodium salt [5, 6] (Fig. 1), a plethora of ruthenium compounds have been developed and assessed for their antitumor activity. Among them, two classes of organometallic half-sandwich Ru(II)–arene species have shown promising anticancer activity in vitro and in vivo. The first group is termed RAPTA and extensive structure–activity relationship studies revealed that the lead compound is $[Ru^{II}(\eta^6\text{-}p\text{-cymene})Cl_2(1,3,5\text{-triaza-7-phosphadamantane})]$ (RAPTA-C, Fig. 1) [7]. The second group termed RAED is of the general formula $[Ru^{II}(\eta^6\text{-arene})(en)X]^+$ (en = ethane-1,2-diamine, X = halide) [8], with representative, lead compounds the RAED-C (Fig. 1) and RM175 [9, 10]. Contrary to the established Pt(II)-based drugs that share a common pharmacological behavior, even the most structurally similar ruthenium compounds exhibit distinct anticancer profiles. Specifically, NAMI-A has been shown to inhibit metastasis [11], whereas the structurally similar KP1019 and IT139 display cytotoxicity against platinum-resistant primary tumors [6, 12]. The same applies to the organometallic Ru(II)-based compounds, with RAPTA-C exhibiting mainly anti-metastatic activity [13, 14], whereas RAEDs are more cytotoxic and active against primary tumors [15].

The exact mechanism of action and the biological target(s) of ruthenium compounds, even of the most thoroughly studied like NAMI-A and KP1019, remain largely unknown [16]. However, it is commonly accepted that the majority of the ruthenium complexes, similar to cisplatin and its analogues, are prodrugs that are activated by aquation (functional compounds), i.e., replacement of one or more ligands by water molecule(s), possibly preceded by reduction/oxidation [17]. The active species are thus the aquated metabolites that eventually bind covalently to the biological target(s). Early reports suggested that interactions with DNA were ultimately responsible for the anticancer activity of ruthenium compounds. In recent years, though, several studies evidenced that DNA is not necessarily the primary and/or the only target, but interactions with intra- and extra-cellular proteins play a crucial role on the observed pharmacological profile [18–20]. In this context, the low cytotoxicity and the anti-metastatic activity of NAMI-A have been ascribed to its interaction with proteins, due to its fast ligand-exchange kinetics that restrains internalization by cells [21]. On the other hand, it has been demonstrated that the increased cytotoxicity of KP1019 arises from its slow extra-cellular degradation that allows enhanced cellular uptake and interaction with DNA [22]. Similarly, RAPTA-C has been shown to target proteins selectively, whereas RAED-C displayed a preference for targeting DNA over proteins [23, 24]. It is, therefore, evident that the peripheral ligands have a considerable impact on the chemical properties of the ruthenium compounds, which determine their target preferences and consequent mechanisms of action.

To assess the function of the η^6-arene ligand of half-sandwich Ru(II) compounds in the context of their anticancer activity, Alessio and co-workers have developed a series of "half sandwich"-type Ru(II) *coordination* compounds. In these compounds, the aromatic fragment was replaced by a neutral, six-electron donor, face-capping ligand (such as 1,4,7-trithiacyclononane, *[9]aneS3*), with the remaining coordination sphere unchanged [25–29]. While the majority of these Ru(II) *coordination* compounds did not reveal any significant anti-proliferative activity, $[Ru^{II}([9]aneS3)(en)Cl]^+$ (RuTE-Cl, i.e., the coordination counterpart of RAEDs, Fig. 1) showed moderate in vitro cytotoxicity, indicating that the arene ligand can be effectively replaced by other face-capping ligands without total loss of activity [26–29]. Interestingly, RuTE-Cl displays chemical behavior in aqueous solutions and DNA-binding properties similar to those of the RAED group of organometallic compounds

[30]. However, the lower cytotoxic activity of RuTE-Cl in comparison to RAEDs has been attributed to its lower lipophilicity (*[9]aneS3* vs arene) and to the faster ligand-exchange kinetics, with the Cl ligand of RuTE-Cl displaying *ca.* tenfold faster hydrolysis rate than RAED-C under the same conditions [30].

The nature of protein–ruthenium adducts at the atomic level has been elucidated by crystallographic studies, which highlight the role and importance of the Ru ligands, and provide clues about a general mode of Ru binding [31–33]. With the aim to obtain structural information on the protein-binding mode of these Ru(II) *coordination* compounds, and towards a better understanding of their mode of action, we studied the crystal structures of the protein adducts formed upon reaction of RuTE-Cl with hen egg-white lysozyme (HEWL) and proteinase K (PK). HEWL (EC 3.2.1.17) is a 129-amino acid residue enzyme (14.3 kDa) and has been extensively employed as a model protein due to its stability over a wide range of conditions. More importantly, HEWL has been employed in several structural studies of metal-based complexes, including ruthenium anticancer compounds [32, 34–36], thus allowing for direct comparisons. PK from the mold *Tritirachium album Limber* (EC 3.4.21.64) is a commonly used, broad-spectrum protease that belongs to the subtilisin peptidase family S8 [37]. It has two binding sites for Ca^{2+} that are not directly involved in the catalytic mechanism, but which are necessary for stability and catalytic efficiency of the enzyme. PK is a suitable structural model for the study of protein metalation, considering its stability under varying conditions and the facile preparation of high-quality diffraction crystals. To the best of our knowledge, the structure of the PK adduct presented herein is the only ruthenium adduct of PK in the literature. Our results provide the evidence of ligand-induced conformational changes in the catalytic cleft of HEWL, required to accommodate the $\{Ru^{II}([9]aneS3)(en)\}^{2+}$ fragment (hereafter RuTE), and illustrate the role of residue-specific hydrophobic/aromatic and hydrogen-bonding interactions. Comparison with other Ru(II)–protein adducts suggests a prominent role of the ligands in site-specific interactions that are driven by electrostatic forces on the surface of the enzymes.

Table 1 Crystallographic data collection and refinement statistics for the two $\{Ru^{II}([9]aneS3)(en)\}^{2+}$ (RuTE) adducts with HEWL and PK. *RMSD* is the root-mean-square deviation and values in parentheses are for the highest resolution shell

	HEWL–RuTE	PK–RuTE
Data collection		
Space group	$P4_32_12$	$P4_32_12$
Wavelength (Å)	1.000	0.976
Cell dimensions (Å)		
a	79.27	67.71
b	79.27	67.71
c	35.91	107.31
Resolution (Å)	35.45–1.395 (1.445–1.395)	47.90–1.372 (1.421–1.372)
R_{pim}	0.027 (0.197)	0.013 (0.052)
$CC_{1/2}$	0.999 (0.939)	0.999 (0.990)
Mean $I/\sigma(I)$	15.0 (3.7)	35.3 (10.4)
Completeness (%)	98.44 (95.35)	98.10 (85.20)
Redundancy	6.6 (6.2)	5.1 (3.6)
Wilson *B*-factor (Å^2)	18.63	10.86
Molecular replacement		
LLG	2488	25,903
TFZ-score	46.5	105.1
Refinement		
Resolution (Å)	35.45–1.395	47.90–1.372
No. unique reflections	23,111	51,561
No. of TLS groups	10	7
R_{work} (%)	22.08	15.19
R_{free} (%)	24.14	16.83
Total number of atoms	1,149	2,378
Protein atoms	1,006	2,053
Solvent molecules	117	267
Ligand molecules	1	2
Average B factors (Å^2)		
Overall	29.1	14.9
Protein	28.1	13.2
Solvent	36.3	25.5
Ligands	30.9	22.6
$RMSD_{bonds}$ (Å)	0.020	0.005
$RMSD_{angles}$ (°)	2.09	0.81
Ramachandran		
Favored (%)	97.6	97.5
Allowed (%)	2.4	2.5
PDB accession code	6TVL	6TXG

Materials and methods

The complex $[Ru^{II}([9]aneS3)(en)Cl][CF_3SO_3]$ (RuTE-Cl) was synthesized as described in the literature [29]. HEWL (L7651) and PK (P2308) were purchased from Sigma and were used without further purification. Crystals of HEWL and PK were grown by vapor diffusion sitting drop method at room temperature and at 289 K, respectively, in 96-well plates (Molecular Dimensions, UK). Lyophilized powder of HEWL was dissolved in water at a final concentration of 20 mg/mL, and 2 µL of the protein solution was mixed with equal parts of reservoir solution containing 0.8–1.5 M sodium chloride and 0.1 M sodium acetate adjusted to pH = 4.5. Tetragonal crystals appeared within the same day and grew to full size within 3 days. Lyophilized powder

of PK was suspended in water at a final concentration of 10 mg/mL, and volumes of 2 µL stock protein solution were mixed with equal parts of reservoir solution containing 0.1 M sodium nitrate and 0.1 M of sodium citrate buffer at pH = 6.5. Tetragonal crystals appeared within 3 days and grew to full size within 2 weeks.

Soaking of HEWL and PK crystals with RuTE-Cl was performed by adding solid aliquots to the crystal drops [38]. A significant coloring of the crystals from colorless to yellow was observed within 10 min after the addition of RuTE-Cl with both enzymes. 1 h after the addition of RuTE-Cl, the crystals were captured in silicon loops (Hampton Research, USA) and cryo-protected by rapid immersion in a solution containing the precipitant and 20% (v/v) 1,2-ethanediol. Subsequently, the crystals were flash frozen in liquid nitrogen and shipped inside a Taylor–Wharton CX100 dry shipper to the synchrotron facility. Crystallographic data sets were collected at 100 K and 1.00-Å wavelength at the beamline X06DA of the Swiss Light Synchrotron (PSI, Villigen, Switzerland) for HEWL–RuTE and at 0.98-Å wavelength at the beamline P13 of PETRA III (EMBL, Hamburg, Germany) for PK–RuTE. The reflections were integrated using MOSFLM of CCP4 [39] for HEWL–RuTE and XDS [40] for PK–RuTE, the space group was determined using POINTLESS, and data merging was performed using SCALA of CCP4 [39].

The structures of HEWL–RuTE and PK–RuTE complexes were solved by molecular replacement with PHASER [41] using the ligand-free structures of HEWL (PDB ID: 193L) [42] and PK (PDB ID: 2ID8) [43] as search models. Both structures were refined with PHENIX [44] using positional refinement and implementing TLS refinement at the final stages. Manual model building and real-space refinement were performed with COOT [45], while the geometric restraints of RuTE-Cl (CCDC Accession Code: 265999) [29] were optimized using eLBOW module of PHENIX. The occupancies of RuTE fragments were freely refined in PHENIX using an unrestraint mode. Specifically, RuTE atoms were assigned with the same residue number to be treated as a single chemical species (molecule A). In the PK–RuTE structure, the alternatively present cluster of calcium or sodium ions along with their coordinating water molecules were grouped together (molecule B). The occupancy of the two species (molecules A and B) was treated as one refinable parameter. The overall geometry of the refined models was very good, with 100% of the residues lying within the Ramachandran favored or allowed regions, while displaying MolProbity [46] scores of 1.56 and 1.24 for HEWL–RuTE and PK–RuTE, respectively (Table 1). The electrostatic potential of the proteins was calculated using APBS with default parameters [47], and mapped onto the solvent-accessible surface area of the proteins at a range of −1 (red for negative) to +1 (blue for positive) using PyMOL.

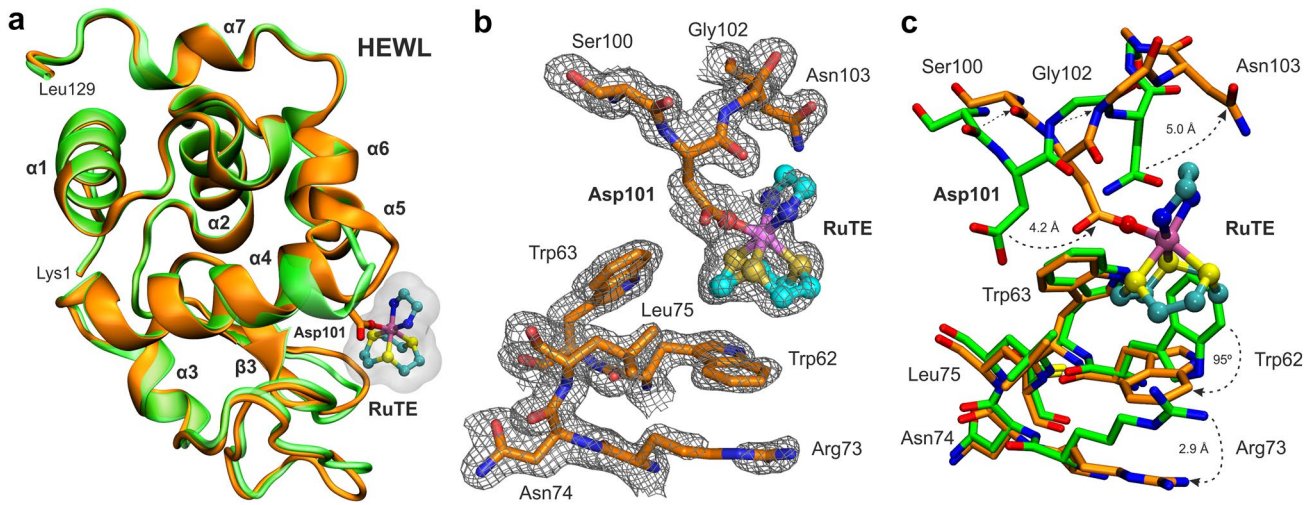

Fig. 2 **a** Cartoon representation of the X-ray crystal structure of HEWL (orange) with the bound RuTE fragment shown with a stick and ball representation (magenta Ru, cyan C, blue N, and yellow S). Superimposed in green cartoon is the ultrahigh-resolution X-ray structure of ligand-free HEWL (PDB ID: 2VB1). The side-chain of the coordinating residue Asp101 is shown as sticks (orange C and red O). **b** Refined electron density of RuTE and of the surrounding HEWL residues, contoured at 1σ. Protein residues and RuTE are colored as in (**a**). **c** Comparison of the residues that display significant conformation changes between the ligand-free (green C) and the RuTE-bound (orange C) HEWL. The values given in Å are the distances between the indicated atoms and the dihedral angle in (°) was calculated between the indole planes of Trp62

Results

The adduct of RuTE with HEWL

Soaking of tetragonal crystals of HEWL with excess of RuTE-Cl resulted in a color change from colorless to yellow within 10 min and the adduct formation was completed within 1 h. The final model of the complex was resolved at 1.40 Å with an average *B* value of 28 Å^2 over all protein atoms. All protein atoms were clearly resolved, with the Cα atoms displaying an average root-mean-square deviation (RMSD) of 0.48 Å from the ultrahigh-resolution crystal structure of ligand-free HEWL (PDB ID: 2VB1) [48]. Backbone and side-chain differences (see below and also Fig. S1) were found mainly at residues 46–47, 70–73, and 99–103 (Fig. 2a and discussion below). The electron density of the RuTE fragment was unambiguously identified (at 90% occupancy and average *B* value of 31 Å^2) bound to the carboxylate side-chain of Asp101 (Fig. 2a). The complex was refined without restraints and the Ru–O bond was found at a length of 1.84 Å, which is relatively shorter compared to the typical range of Ru–Obond lengths of 2.0–2.6 Å (from Ru^{II} coordinated by Asp residues of HEWL, see the Discussion section). Both Ru–N bond lengths were 2.04 Å and the three Ru–S bond lengths were in the range of 2.19–2.24 Å. The geometry around the metal ion is mostly octahedral, with all L–Ru–L angles deviating less than 8° from the orthogonal values, except for the equatorial O–Ru–S angle of 163° (Fig. 2b). At this binding site, the RuTE ligands are sandwiched between Asn103 and Trp62. In particular, one of the N atoms of the *en* ligand is at 3.55 Å from the side-chain NH_2 amide of Asn103 and is hydrogen bonded to a solvent molecule, whereas the other N atom is at 3.43 Å from the backbone C=O of Asp101. On the other side of the complex, the *[9]aneS3* ligand is accommodated within an aromatic, hydrophobic pocket/patch comprised of Trp62, Trp63, and Leu75 (Fig. 2b). All methylene groups of *[9]aneS3* are engaged in CH_2–aromatic interactions with the indole ring of Trp62 (within 3.5–5.0 Å distance). Two of the *[9]aneS3* methylene groups also interact with the side-chain of Trp63, one of which displays an additional hydrophobic interaction with the C^{δ1} methyl group of Leu75.

Interestingly, comparison of the HEWL–RuTE adduct with the ultrahigh-resolution (0.65 Å) structure of ligand-free HEWL [48] revealed that binding of the complex induces significant conformational changes (Fig. 2c). In particular, the side-chains of Asp101 and Asn103 move outwards to coordinate Ru(II) and accommodate the *en* ligand, respectively, with a concomitant main-chain shift of residues 99–103 ($RMSD_{Cα}$ of 1.4–2.8 Å with respect to the ligand-free HEWL). Moreover, the side-chain of Trp62 is rotated by more than 90° to accommodate the *[9]aneS3* ligand of RuTE, as in the case of HEWL with a bound substrate model [49]. Trp62, which has been shown to play a key role in substrate binding, usually displays poor electron density in the crystal structures of the native enzyme due to its flexibility. In contrast, RuTE binding and stacking of the *[9]aneS3* against Trp62 and Trp63 results in stabilization of the two residues, as evidenced by their strong electron density. It should be noted that in the ultrahigh-resolution HEWL structure, Trp62 was found in a double conformation with an angle of 25° between the two indole planes [48]. The conformational change of Trp62 in our structure is also accompanied by a significant side-chain motion of Arg73 (Fig. 2c).

The adduct of RuTE with PK

The adduct of PK with RuTE was formed within 1 h by soaking crystals of PK in excess of RuTE-Cl. The structure was resolved at 1.37 Å with an average *B* value of 15 Å^2 over all atoms (13 Å^2 protein only atoms), which is almost identical to the atomic resolution X-ray structures of ligand-free PK (PDB IDs: 1IC6 [50] and 5KXV [51]), displaying C^α atom RMSDs of less than 0.1 Å (Fig. S2). The extra-electron density found at the two Ca^{2+}-binding sites was assigned to two RuTE fragments bound to Asp200 at site 1 (0.54 occupancy and average $B = 21$ Å^2) and Asp260 at site 2 (0.39 occupancy and average $B = 24$ Å^2), as shown in Fig. 3. The remaining density was assigned to a Ca^{2+} ion and two water molecules at site 1 (occupancy of 0.46) and a Na^+ ion and three water molecules at site 2 (occupancy of 0.61). The residual electron density of site 2, which is known to be weak Ca^{2+}-binding site, was also recognized as a sodium ion on the basis of its coordination geometry [52].

RuTE at site 2 is coordinated to O^{δ1} of Asp260 (Ru–O bond unrestrained refined at a length of 2.25 Å), while O^{δ2} of Asp260 was found at a distance of 2.60 Å from one NH_2 (Fig. 3a, b). The same NH_2 is hydrogen-bonded to the backbone carbonyl of Thr16, whereas the other N of *en* is at a distance of 3.6 Å from the carbonyl of Lys258. The *[9]aneS3* ligand of RuTE (site 2) is mainly exposed to the solvent. As a result, while the sulfur atoms of the ligand are well localized in geometrically ideal positions, the bridging ethylene groups are only weakly resolved in the unbiased *Fo–Fc* difference maps (Fig S3c). RuTE at site 1 is bound to the carboxylate group of Asp200, with a Ru–Obond length of 2.05 Å and an equatorial O–Ru–S angle of 176° (Fig. 3d). One of the NH_2 groups of *en* is stabilized by two hydrogen bonds with the main-chain carbonyl groups of Pro175 and Val177, whereas the other is hydrogen-bonded to a solvent molecule only (Fig. 3a). The *[9]aneS3* ligand of RuTE (site 1) exhibits only a few contacts with the side-chains of Pro175 and Val269 (at 4.1–4.6 Å). Still, these contacts stabilize the ligand enough to be sufficiently resolved in the

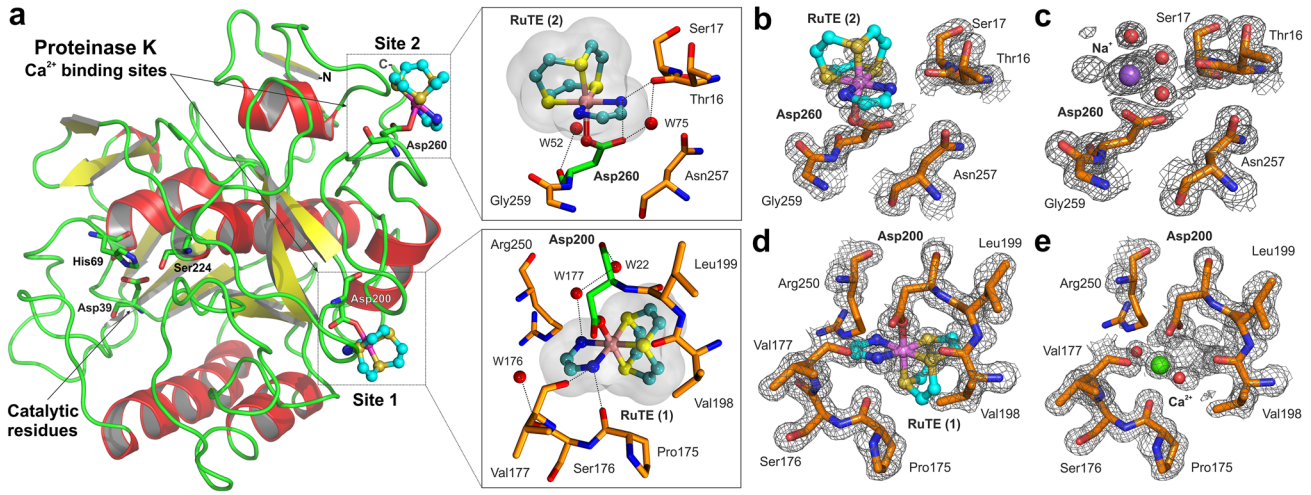

Fig. 3 **a** Cartoon illustration of the X-ray structure of PK with the bound RuTE fragments at the two calcium-binding sites of the enzyme. The coordinating residues Asp200 and Asp260, as well as the catalytic triad residues in the active site of PK are shown with green C sticks. Inset are close-up views of the two RuTE-binding sites, with hydrogen-bonding interactions indicated by dotted lines. **b** Refined electron density of RuTE bound to Asp260 at the Ca^{2+}-binding site 2 (assigned with an occupancy of 0.4) and surrounding residues contoured at 1σ. **c** Alternative occupancy of site 2 was attributed to a Na^{+} cation that is coordinated by three water molecules and Asp260. **d** Refined electron density of RuTE coordinated to Asp200 in the Ca^{2+}-binding site 1 (occupancy of 0.5) and surrounding residues contoured at 1σ. **e** Alternative occupancy of site 1 was assigned to a Ca^{2+} ion and two water molecules

Fo–Fc difference maps (Fig. S3b). The Ru–Obond lengths in the protein adducts were determined without using any restraints and were found to be within the typical range (2.05 Å in RuTE at site 1 and 2.25 Å at site 2).

The two RuTE adducts are bound to PK without causing any significant conformational change to the Ca^{2+}-binding site residues (Fig. S4). At site 1, the Ru(II)-bound side-chain of Asp200 is practically at the same position as in the ligand-free enzyme, where the position of Ca^{2+} is occupied by one of the N atoms of the *en* ligand. The alternative occupancy (0.46) was attributed to a Ca^{2+} and two water molecules (Fig. 3e). Similarly, binding of RuTE at site 2 mediates a minor movement of Asp260 and the displacement of the four Ca^{2+}-bound water molecules, with the N1 of *en* close to the position of the calcium cation. However, the alternative occupancy of site 2 (0.61) was assigned to a Na^{+} ion, which is coordinated to Asp260 and three solvent molecules in a trigonal pyramidal arrangement (Fig. 3c). These observations are in accordance with the previous studies, which showed that one calcium ion binds tightly (pK 7.6×10^{-8} M^{-1}) and the other binds only weakly [53], whereas a sodium ion can occupy a PK calcium-binding site under Ca^{2+}-free conditions [54]. Removal of the calcium ions (e.g., using EDTA) results in ~ 80% decrease of PK activity within 3 h, which has been attributed to subtle structural changes of the enzyme and of its hydration properties [53].

Discussion

Recent studies of two Ru(II)-arene compounds have demonstrated that RAPTA-C and RAED-C (Fig. 1) target chromatin with different site selectivity [23, 24]. While RAPTA-C is primarily associated with the histone proteins, RAED-C preferentially targets the DNA component of chromatin, albeit sharing some common histone-binding sites. The different selectivity of RAPTA-C and RAED-C was mainly attributed to steric constraints of the bulky phosphaadamantane ligand of RAPTA-C within DNA, and this has been correlated with their distinct cytotoxicity profiles. While RAED-C exhibits high cytotoxicity and activity against primary tumors that is comparable to cisplatin, RAPTA-C displays low cytotoxicity, but has been shown to have anti-angiogenic and anti-metastatic properties [13, 14]. Therefore, it has been suggested that modifications in ligand structure or coordination ability of Ru(II) compounds can modulate their DNA/protein-targeting activity, and thus their cytotoxic potential. With the aim to provide structural evidence on the role of the ligands in protein binding, we employed a Ru(II) *coordination* compound, RuTE-Cl, in which the arene fragment of the RAEDs is substituted by the face-capping *[9]aneS3* ligand (Fig. 1).

Treatment of HEWL crystals with RuTE-Cl revealed a single adduct at the side-chain of Asp101 (Fig. 2). Upon hydrolysis of the chloride ligand, the positively (+2*e*) charged RuTE species binds to the carboxylate group of Asp101. Binding of RuTE mediates a conformational

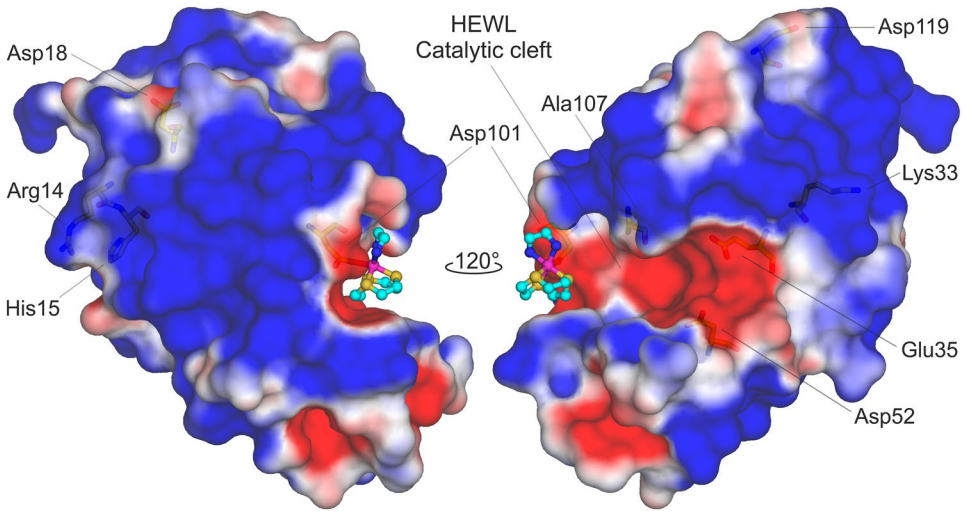

Fig. 4 Solvent accessible surface of the HEWL–RuTE crystal structure colored by electrostatic potential. The Asp101-bound RuTE adduct and other ruthenation sites that have been identified on HEWL, including the two catalytic residues of the enzyme (Glu35 and Asp52), are indicated. Atom colors are as in Fig. 2

change at the catalytic cleft, similar to that observed in the substrate-receptive conformation of HEWL (Fig. 2c). The *en* ligand is accommodated by a shift in the side-chain of Asn103, whereas the *[9]aneS3* ligand is stacked over the indole ring of Trp62, exhibiting several methylene–aromatic interactions, and is also in contact with Trp63 and Leu75 (Fig. 2b). An examination of the electrostatic potential surface of HEWL reveals that although the enzyme comprises an overall positively charged surface, the site of ruthenation by RuTE occurs at the basic site of Asp101, which is part of the catalytic cleft comprising also the active site residues Glu35 and Asp52 (Fig. 4).

For the purpose of comparison with related structures of Ru(II)–HEWL adducts, the first crystal structure of a Ru(II)–arene adduct revealed that the neutral $[Ru^{II}(\eta^6\text{-}p\text{-cymene})Cl_2(H_2O)]$ species forms a single adduct that is coordinated by $N^{\varepsilon 1}$ of His15, the only histidine residue of HEWL [34]. At this site, the neutral Ru(II) fragment is bound at a positively charged patch (Fig. 4), with the arene group displaying contacts with the side-chains of Lys14 and Asp87. It should be noted, however, that ICP-MS analysis has indicated more than one ruthenation sites on HEWL [34]. A more recent crystallographic study of HEWL metalation by dinuclear organometallic complexes of the formula $[M(\eta^6\text{-}p\text{-cymene})X_2]_2$ [M = Ru(II) or Os(II), X = halide] has revealed a selective interaction of the neutral $\{M(\eta^6\text{-}p\text{-cymene})Cl_2\}$ fragment with His15, which was independent of the metal center or the halide [32]. Interestingly, a second binding site was found, where the positively charged $\{(\eta^6\text{-}p\text{-cymene})Ru(\mu\text{-}Cl_2)Ru\}^{3+}$ fragment was coordinated by Asp101 that bridged the two Ru centers. Although this binding site was suggested to be weaker, as the complex was refined with 0.5 occupancy, this observation provides evidence that most likely the ligand-induced charge of the Ru fragments can modulate the selectivity of the metalation site. In a later work, the same group presented the first X-ray structure of a Ru–carbene adduct of HEWL using $[Ru^{II}(\eta^6\text{-}p\text{-cymene})(dmb)Cl_2]$ (dmb = 1,3-dimethylbenzimidazol-2-ylidene), where three distinct binding sites were identified [33]. In the first site, $\{RuCl_2(dmb)(OH_x)\}$ was coordinated to both side-chains of Arg14 and His15, whereas at the second site, an adduct of $\{RuCl_2(dmb)(OH_x)_2\}$ with the side-chain amine of Lys33 was formed. A third site was identified with a $\{RuCl(OH_x)_4\}$ fragment displaying weak interactions with the carbonyl oxygen of Ala107 [33]. Although the overall charge of the Ru adducts could not be unambiguously determined (the metal center has been shown to be oxidized upon exchange of the arene ligand, and the nature of the coordinated H_2O vs OH^- has not been determined), and thus, no correlation between fragment's charge and site selectivity can be extracted; these results clearly show that different fragments target diverse sites.

Similarly, HEWL adducts with carbon monoxide-releasing compounds have revealed multiple ruthenation sites, with His15 recognized as the primary site. In particular, soaking of HEWL with *fac*-$[Ru^{II}(CO)_3Cl(\kappa^2\text{-}H_2NCH_2CO_2)]$ resulted in three adducts of the *cis*-$\{Ru^{II}(CO)_2(H_2O)_3\}^{2+}$ fragment bound to His15, Asp18, and Asp52 with occupancies of 0.8, 0.5, and 0.4, respectively [55]. In a subsequent work, reaction of HEWL with a series of ruthenium carbonyl complexes of the general formula *fac*-$[Ru^{II}(CO)_3Cl_2L]$ (L = neutral monodentate ligand) revealed multiple ruthenation sites, still exhibiting His15 as the primary site of interaction (occupancies of 0.7–1.0), and with Asp18, Asp52, Asp101, and Asp119 identified as secondary sites (occupancies of 0.4–0.7) [56]. A more recent crystallographic study of Ru(II) carbonyl complexes of the same general formula, where L = N^3-imidazole or N^3-methyl-imidazole [57], revealed that upon dissociation of the azole ligand,

the two chlorides and one or two CO molecules, the complexes bind HEWL at His or Asp residues (His15, Asp18, Asn46 and Asp52, Asp119 and Arg125, or the C-terminus of Leu129) [58]. For all the HEWL adducts studied, His15 was identified as the highest occupancy ruthenation site, followed by Asp18 (a detailed table can be found in the supplementary information of ref. 58). On the other hand, reaction of the mixed-valence diruthenium(II,III) complex $[Ru_2(\mu\text{-}O_2CCH_3)_4Cl]$ with HEWL revealed two adducts of the $\{Ru_2(\mu\text{-}O_2CCH_3)_2\}^{3+}$ fragment bound to Asp101 and Asp119, with their carboxylate groups bridging the two metal centers [59].

The above observations, taken together with an examination of the ruthenation sites on the electrostatic potential surface of HEWL (Fig. 4), suggest that neutral species, such as the $\{Ru^{II}(\eta^6\text{-}p\text{-cymene})Cl_2\}$ fragments, are preferentially coordinated by the heterocyclic N atom of His, which is located at a positively charged site. On the other hand, positively charged species, such as RuTE and the diruthenium organometallic compounds, display a preference for the O atom donors of aspartate residues that are located at negatively charged sites on the surface of HEWL. In cases where positively charged Ru(II) species were coordinated by His15, such as for the $\{Ru^{II}(CO)_x\}$ adducts, alternative ruthenation sites were identified at negatively charged aspartate residues (Fig. 4). Interestingly, from the plethora of potential ruthenation sites identified on HEWL, RuTE displays a strong preference for Asp101 under the conditions studied.

These observations are further supported by the second crystal structure of the unrelated enzyme PK (Fig. 3), in which the ruthenation sites coincide with the two calcium-binding sites of the enzyme. Our data show that the two RuTE fragments are coordinated by the carboxylate groups of Asp200 and Asp260, without causing any significant conformational change of PK. The two RuTE adducts are further stabilized through hydrogen-bonding interactions between the *en* ligands and main-chain atoms from the surrounding residues (Fig. 3b). Examination of the electrostatic potential surface of PK reveals that the two Ca^{2+}-binding sites are regions of negatively charged electrostatic potential (Fig. 5). In particular, the well-defined site 1 where the highest occupancy RuTE adduct was identified, displays also the highest negatively charged potential. In the second, less well-defined Ca^{2+}-binding site, the RuTE adduct was resolved at a lower fraction of the total occupancy. While we cannot make a direct comparison with the other X-ray structures, as this is the first crystal structure of a ruthenated PK adduct, our observations are in accordance with the results obtained from the crystallographic studies of Ru(II)–arene adducts with the nucleosome core particle [23, 24]. Albeit their different DNA/protein selectivity that has been attributed to the steric demands of the bulkier ligands, RAPTA-C and RAED-C (Fig. 1) have been shown to share a single common binding site on the histone proteins. At this site (designated as Site 2 in Fig. S5), the positively charged Ru(II)–arene fragments were coordinated by Glu carboxylate groups within a highly acidic cleft formed by the histone H2A–H2B dimer. Even though the coordinating ligands of RAPTA-C and RAED-C are different at the variable sites of interaction with chromatin, still, the electrostatic forces appear as the steering force of the positively charged species towards regions of negatively charged potential, as in the case of the PK–RuTE adducts presented here (Fig. 5).

Conclusions

While the previous studies have investigated the protein ruthenation by means of organometallic half-sandwich Ru(II) compounds with arene ligands, the present study concentrates on a coordination analogue to RAED, namely $[Ru^{II}([9]aneS3)(en)Cl]^+$ (RuTE-Cl), that bears a face-capping crown thioether ligand (i.e., *[9]aneS3*) in place of the arene. In this sense, we provide the first structural insights

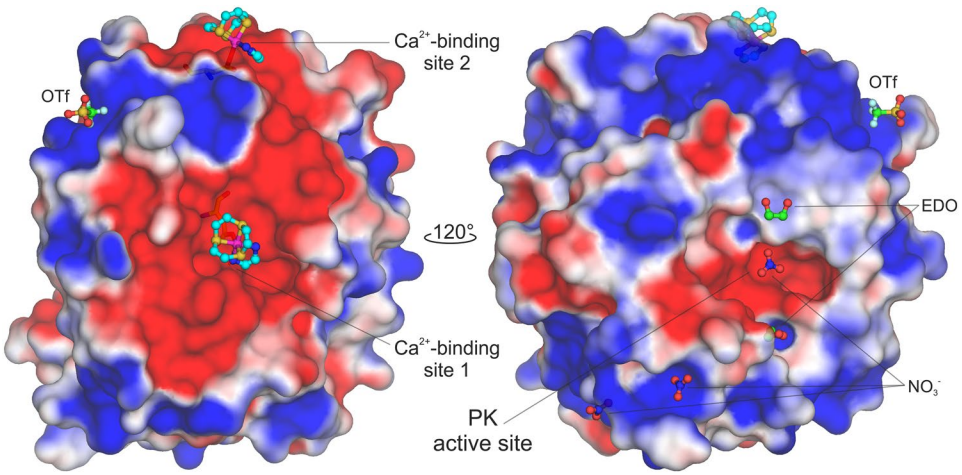

Fig. 5 Solvent accessible surface of the HEWL–RuTE crystal structure colored by electrostatic potential. The two RuTE adducts, a triflate counter ion (OTf), two ethylene glycol molecules (EDO), and three nitrate ions are shown as ball-and-sticks and are colored as in Fig. 2. The two Ca^{2+}-binding sites and the active site of the enzyme are indicated

for the protein adducts formed by this "half sandwich"-type Ru(II) *coordination* compound with two model proteins (i.e., HEWL and PK). These X-ray structures are also the first examples, to the best of our knowledge, of adducts between proteins and Ru(II) *coordination* compounds that maintain their coordination sphere almost intact. Typically, Ru was found as a naked ion when coordination compounds were used (e.g., NAMI-A and KP1019). In the HEWL adduct, RuTE is coordinated by Asp101 at the side of the catalytic cavity, whereas in the PK adduct, RuTE is coordinated at the two calcium-binding sites of the enzyme. In the case of HEWL, conformational rearrangements of the surrounding residues were detected, whereas the two RuTE fragments bind at PK without causing any conformational change. The HEWL–RuTE adduct is stabilized mainly via hydrophobic/aromatic interactions of the *[9]aneS3* ligand, whereas the PK–RuTE adducts display hydrogen-bonding interactions of the *en* ligand with main-chain residues. Taken together, our analysis suggests that although the hydrophobic forces underpin the dominant interactions between the ligands and protein residues, in accordance with many structural studies of protein–ruthenium adducts, the overall charge of the complex, dictated by its coordination sphere, underlies the steering force towards electrostatically favorable regions on protein surfaces.

Acknowledgements We would like to thank Prof. Enzo Alessio and the reviewers for their constructive comments on the manuscript. We would also like to thank the beamline scientists at the synchrotron facilities of the Swiss Light Source at PSI, (Villigen, Switzerland) and of PETRA III at EMBL (Hamburg, Germany) for their assistance during X-ray data collection. This work was supported by the project "INSPIRED" (Grant MIS 5002550).

Compliance with ethical standards

Conflict of interest The authors declare that they have no conflict of interest.

References

1. Alessio E (2011) Bioinorganic medicinal chemistry. Wiley-VCH Verlag GmbH & Co. KGaA, Weinheim, Germany. doi: 10.1002/9783527633104
2. Monro S, Colón KL, Yin H, Roque J, Konda P, Gujar S, Thummel RP, Lilge L, Cameron CG, McFarland SA (2019) Transition metal complexes and photodynamic therapy from a tumor-centered approach: challenges, opportunities, and highlights from the development of TLD1433. Chem Rev 119(2):797–828
3. Rademaker-Lakhai JM, Van Den Bongard D, Pluim D, Beijnen JH, Schellens JHM (2004) A phase I and pharmacological study with imidazolium-trans-DMSO-imidazole-tetrachlororuthenate, a novel ruthenium anticancer agent. Clin Cancer Res 10(11):3717–3727
4. Lentz F, Drescher A, Lindauer A, Henke M, Hilger RA, Hartinger CG, Scheulen ME, Dittrich C, Keppler BK, Jaehde U (2009) Pharmacokinetics of a novel anticancer ruthenium complex (KP1019, FFC14A) in a phase i dose-escalation study. Anticancer Drugs 20(2):97–103
5. Burris HA, Bakewell S, Bendell JC, Infante J, Jones SF, Spigel DR, Weiss GJ, Ramanathan RK, Ogden A, Von Hoff D (2016) Safety and activity of IT-139, a ruthenium-based compound, in patients with advanced solid tumours: a first-in-human, open-label, dose-escalation phase i study with expansion cohort. ESMO Open 1(6):e000154
6. Trondl R, Heffeter P, Kowol CR, Jakupec MA, Berger W, Keppler BK (2014) NKP-1339, the first ruthenium-based anticancer drug on the edge to clinical application. Chem Sci 5(8):2925–2932
7. Murray BS, Babak MV, Hartinger CG, Dyson PJ (2016) The development of RAPTA compounds for the treatment of tumors. Coord Chem Rev 306(P1):86–114
8. Yan YK, Melchart M, Habtemariam A, Sadler PJ (2005) Organometallic chemistry, biology and medicine: ruthenium arene anticancer complexes. Chem Commun 38:4764–4776
9. Aird RE, Cummings J, Ritchie AA, Muir M, Jodrell DI, Morris RE, Chen H, Sadler PJ (2002) In vitro and in vivo activity and cross resistance profiles of novel ruthenium (II) organometallic arene complexes in human ovarian cancer. Br J Cancer 86(10):1652–1657
10. Bergamo A, Masi A, Peacock AFA, Habtemariam A, Sadler PJ, Sava G (2010) In vivo tumour and metastasis reduction and in vitro effects on invasion assays of the ruthenium RM175 and osmium AFAP51 organometallics in the mammary cancer model. J Inorg Biochem 104(1):79–86
11. Bergamo A, Sava G (2015) Linking the future of anticancer metal-complexes to the therapy of tumour metastases. Chem Soc Rev 44(24):8818–8835
12. Hartinger CG, Zorbas-Seifried S, Jakupec MA, Kynast B, Zorbas H, Keppler BK (2006) From bench to bedside—preclinical and early clinical development of the anticancer agent indazolium trans-[tetrachlorobis(1*H*-indazole)ruthenate(III)] (KP1019 or FFC14A). J Inorg Biochem 100(5–6):891–904
13. Scolaro C, Bergamo A, Brescacin L, Delfino R, Cocchietto M, Laurenczy G, Geldbach TJ, Sava G, Dyson PJ (2005) In vitro and in vivo evaluation of ruthenium(II)-arene PTA complexes. J Med Chem 48(12):4161–4171
14. Nowak-Sliwinska P, Van Beijnum JR, Casini A, Nazarov AA, Wagnières G, Van Den Bergh H, Dyson PJ, Griffioen AW (2011) Organometallic ruthenium(II) arene compounds with antiangiogenic activity. J Med Chem 54(11):3895–3902
15. Guichard SM, Else R, Reid E, Zeitlin B, Aird R, Muir M, Dodds M, Fiebig H, Sadler PJ, Jodrell DI (2006) Anti-tumour activity in non-small cell lung cancer models and toxicity profiles for novel ruthenium(II) based organo-metallic compounds. Biochem Pharmacol 71(4):408–415
16. Alessio E (2017) Thirty years of the drug candidate NAMI-A and the myths in the field of ruthenium anticancer compounds: a personal perspective. Eur J Inorg Chem 2017(12):1549–1560
17. Gianferrara T, Bratsos I, Alessio E (2009) A categorization of metal anticancer compounds based on their mode of action. Dalton Trans 37:7588–7598
18. Meier-Menches SM, Gerner C, Berger W, Hartinger CG, Keppler BK (2018) Structure-activity relationships for ruthenium and osmium anticancer agents-towards clinical development. Chem Soc Rev 47(3):909–928
19. Messori L, Merlino A (2017) Protein metalation by metal-based drugs: X-ray crystallography and mass spectrometry studies. Chem Commun 53(85):11622–11633
20. Rilak Simović A, Masnikosa R, Bratsos I, Alessio E (2019) Chemistry and reactivity of ruthenium(II) complexes: DNA/protein

binding mode and anticancer activity are related to the complex structure. Coord Chem Rev 398:113011
21. Aitken JB, Antony S, Weekley CM, Lai B, Spiccia L, Harris HH (2012) Distinct cellular fates for KP1019 and NAMI-A determined by X-ray fluorescence imaging of single cells. Metallomics 4(10):1051–1056
22. Levina A, Aitken JB, Gwee YY, Lim ZJ, Liu M, Singharay AM, Wong PF, Lay PA (2013) Biotransformations of anticancer ruthenium(III) complexes: an X-ray absorption spectroscopic study. Chem Eur J 19(11):3609–3619
23. Adhireksan Z, Davey GE, Campomanes P, Groessl M, Clavel CM, Yu H, Nazarov AA, Yeo CHF, Ang WH, Dröge P, Rothlisberger U, Dyson PJ, Davey CA (2014) Ligand substitutions between ruthenium–cymene compounds can control protein versus DNA targeting and anticancer activity. Nat Commun 5(1):3462
24. Wu B, Ong MS, Groessl M, Adhireksan Z, Hartinger CG, Dyson PJ, Davey CA (2011) A ruthenium antimetastasis agent forms specific histone protein adducts in the nucleosome core. Chem Eur J 17(13):3562–3566
25. Bratsos I, Birarda G, Jedner S, Zangrando E, Alessio E (2007) Half-sandwich Ru^{II}-[9]aneS_3 complexes with dicarboxylate ligands: synthesis, characterization and chemical behavior. Dalton Trans 36:4048–4058
26. Bratsos I, Jedner S, Bergamo A, Sava G, Gianferrara T, Zangrando E, Alessio E (2008) Half-sandwich Ru^{II}-[9]aneS_3 complexes structurally similar to antitumor-active organometallic piano-stool compounds: Preparation, structural characterization and in vitro cytotoxic activity. J Inorg Biochem 102(5–6):1120–1133
27. Bratsos I, Mitri E, Ravalico F, Zangrando E, Gianferrara T, Bergamo A, Alessio E (2012) New half sandwich Ru(II) coordination compounds for anticancer activity. Dalton Trans 41(24):7358–7371
28. Kljun J, Bratsos I, Alessio E, Psomas G, Repnik U, Butinar M, Turk B, Turel I (2013) New uses for old drugs: attempts to convert quinolone antibacterials into potential anticancer agents containing ruthenium. Inorg Chem 52(15):9039–9052
29. Serli B, Zangrando E, Gianferrara T, Scolaro C, Dyson PJ, Bergamo A, Alessio E (2005) Is the aromatic fragment of piano-stool ruthenium compounds an essential feature for anticancer activity? The development of new Ru^{II}-[9]aneS_3 analogues. Eur J Inorg Chem 17:3423–3434
30. Rilak A, Bratsos I, Zangrando E, Kljun J, Turel I, Bugarčić ŽD, Alessio E (2012) Factors that influence the antiproliferative activity of half sandwich RuII-[9]aneS3 coordination compounds: activation kinetics and interaction with guanine derivatives. Dalton Trans 41(38):11608–11618
31. Merlino A (2016) Interactions between proteins and Ru compounds of medicinal interest: a structural perspective. Coord Chem Rev 326:111–134
32. Sullivan MP, Groessl M, Meier SM, Kingston RL, Goldstone DC, Hartinger CG (2017) The metalation of hen egg white lysozyme impacts protein stability as shown by ion mobility mass spectrometry, differential scanning calorimetry, and X-ray crystallography. Chem Commun 53(30):4246–4249
33. Sullivan MP, Nieuwoudt MK, Bowmaker GA, Lam NYS, Truong D, Goldstone DC, Hartinger CG (2018) Unexpected arene ligand exchange results in the oxidation of an organoruthenium anticancer agent: the first X-ray structure of a protein-Ru(carbene) adduct. Chem Commun 54(48):6120–6123
34. McNae IW, Fishburne K, Habtemariam A, Hunter TM, Melchart M, Wang F, Walkinshaw MD, Sadler PJ (2004) Half-sandwich arene ruthenium(II)-enzyme complex. Chem Commun 10(16):1786–1787
35. Messori L, Merlino A (2014) Ruthenium metalation of proteins: the X-ray structure of the complex formed between NAMI-A and hen egg white lysozyme. Dalton Trans 43(16):6128–6131
36. Sullivan MP, Nieuwoudt MK, Bowmaker GA, Lam NYS, Truong D, Goldstone DC, Hartinger CG (2018) Unexpected arene ligand exchange results in the oxidation of an organoruthenium anticancer agent: the first X-ray structure of a protein-Ru(carbene) adduct. Chem Commun 54(48):6120–6123 (Correction: Chem Commun (2019) 55(5):716)
37. Bajorath J, Hinrichs W, Saenger W (1988) The enzymatic activity of proteinase K is controlled by calcium. Eur J Biochem 176(2):441–447
38. Russo Krauss I, Ferraro G, Pica A, Márquez JA, Helliwell JR, Merlino A (2017) Principles and methods used to grow and optimize crystals of protein-metallodrug adducts, to determine metal binding sites and to assign metal ligands. Metallomics 9(11):1534–1547
39. Winn MD, Ballard CC, Cowtan KD, Dodson EJ, Emsley P, Evans PR, Keegan RM, Krissinel EB, Leslie AGW, McCoy A, McNicholas SJ, Murshudov GN, Pannu NS, Potterton EA, Powell HR, Read RJ, Vagin A, Wilson KS (2011) Overview of the CCP4 suite and current developments. Acta Crystallogr D Biol Crystallogr 67(4):235–242
40. Kabsch W (2010) XDS. Acta Crystallogr Sect D Biol Crystallogr 66(2):125–132
41. McCoy AJ, Grosse-Kunstleve RW, Adams PD, Winn MD, Storoni LC, Read RJ (2007) Phaser crystallographic software. J Appl Crystallogr 40(4):658–674
42. Vaney MC, Maignan S, Riès-Kautt M, Ducruix A (1996) High-resolution structure (1.33 Å) of a HEW lysozyme tetragonal crystal grown in the APCF apparatus. Data and structural comparison with a crystal grown under microgravity from spaceHab-01 mission. Acta Crystallogr Sect D Biol Crystallogr 52(3):505–517
43. Wang J, Dauter M, Dauter Z (2006) What can be done with a good crystal and an accurate beamline? Acta Crystallogr D Biol Crystallogr 62(12):1475–1483
44. Afonine PV, Grosse-Kunstleve RW, Echols N, Headd JJ, Moriarty NW, Mustyakimov M, Terwilliger TC, Urzhumtsev A, Zwart PH, Adams PD (2012) Towards automated crystallographic structure refinement with phenix.refine. Acta Crystallogr Sect D Biol Crystallogr 68(4):352–367
45. Emsley P, Cowtan K (2004) Coot: Model-building tools for molecular graphics. Acta Crystallogr Sect D Biol Crystallogr 60(12 I):2126–2132
46. Chen VB, Arendall Iii WB, Headd JJ, Keedy DA, Immormino RM, Kapral GJ, Murray LW, Richardson JS, Richardson DC (2010) MolProbity: all-atom structure validation for macromolecular crystallography. Acta Crystallogr D Biol Crystallogr 66(1):12–21
47. Baker NA, Sept D, Joseph S, Holst MJ, McCammon JA (2001) Electrostatics of nanosystems: application to microtubules and the ribosome. Proc Natl Acad Sci 98(18):10037–10041
48. Wang J, Dauter M, Alkire R, Joachimiak A, Dauter Z (2007) Triclinic lysozyme at 0.65 Å resolution. Acta Crystallogr Sect D Biol Crystallogr 63(12):1254–1268
49. Vocadlo DJ, Davies GJ, Laine R, Withers SG (2001) Catalysis by hen egg-white lysozyme proceeds via a covalent intermediate. Nature 412(6849):835–838
50. Betzel C, Gourinath S, Kumar P, Kaur P, Perbandt M, Eschenburg S, Singh TP (2001) Structure of a serine protease proteinase K from Tritirachium album limber at 0.98 Å resolution. Biochemistry 40(10):3080–3088
51. Masuda T, Suzuki M, Inoue S, Song C, Nakane T, Nango E, Tanaka R, Tono K, Joti Y, Kameshima T, Hatsui T, Yabashi M, Mikami B, Nureki O, Numata K, Iwata S, Sugahara M (2017) Atomic resolution structure of serine protease proteinase K at ambient temperature. Sci Rep 7:45604
52. Zheng H, Cooper DR, Porebski PJ, Shabalin IG, Handing KB, Minor W (2017) CheckMyMetal: a macromolecular metal-binding validation tool. Acta Crystallogr Sect D Struct Biol 73:223–233
53. Bajorath J, Raghunathan S, Hinrichs W, Saenger W (1989) Long-range structural changes in proteinase K triggered by calcium ion removal. Nature 337(6206):481–484

54. Muller A, Hinrichs W, Wolf WM, Saenger W (1994) Crystal structure of calcium-free proteinase K at 1.5-Å resolution. J Biol Chem 269(37):23108–23111
55. Santos-Silva T, Mukhopadhyay A, Seixas JD, Bernardes GJL, Romão CC, Romão MJ (2011) CORM-3 reactivity toward proteins: the crystal structure of a Ru(II) dicarbonyl-lysozyme complex. J Am Chem Soc 133(5):1192–1195
56. Seixas JD, Santos MFA, Mukhopadhyay A, Coelho AC, Reis PM, Veiros LF, Marques AR, Penacho N, Gonçalves AML, Romão MJ, Bernardes GJL, Santos-Silva T, Romão CC (2015) A contribution to the rational design of $Ru(CO)_3Cl_2L$ complexes for in vivo delivery of CO. Dalton Trans 44(11):5058–5075
57. Tamasi G, Merlino A, Scaletti F, Heffeter P, Legin AA, Jakupec MA, Berger W, Messori L, Keppler BK, Cini R (2017) {Ru(CO)x}-Core complexes with benzimidazole ligands: synthesis, X-ray structure and evaluation of anticancer activity in vivo. Dalton Trans 46(9):3025–3040
58. Pontillo N, Ferraro G, Messori L, Tamasi G, Merlino A (2017) Ru-Based CO releasing molecules with azole ligands: interaction with proteins and the CO release mechanism disclosed by X-ray crystallography. Dalton Trans 46(29):9621–9629
59. Messori L, Marzo T, Sanches RNF, Hanif Ur R, De Oliveira SD, Merlino A (2014) Unusual structural features in the lysozyme derivative of the tetrakis(acetato)chloridodiruthenium(ii, iii) complex. Angew Chem Int Ed 53(24):6172–6175